

# Analysis of a random modulation single photon counting differential absorption lidar system for space-borne atmospheric CO<sub>2</sub> sensing

X. AI,<sup>1,\*</sup> A. PÉREZ-SERRANO,<sup>2</sup> M. QUATREVALET,<sup>3</sup> R. W. NOCK,<sup>1,4</sup>  
N. DAHNOUN,<sup>1</sup> G. EHRET,<sup>3</sup> I. ESQUIVIAS,<sup>2</sup> AND J. G. RARITY<sup>1</sup>

<sup>1</sup>*Dept. of Electrical and Electronic Engineering, University of Bristol, Merchant Venturers Building, Woodland Road, Bristol BS8 1UB, UK*

<sup>2</sup>*CEMDATIC-E.T.S.I. Telecomunicación, Universidad Politécnica de Madrid, Avda. Complutense 30, 28040 Madrid, Spain*

<sup>3</sup>*Institut für Physik der Atmosphäre, Deutsches Zentrum für Luft- und Raumfahrt (DLR) Oberpfaffenhofen, Münchner Straße 20, 82234 Weßling, Germany*

<sup>4</sup>*Faculty of Computing, Engineering and the Built Environment, Birmingham City University, Millennium Point, Curzon Street, Birmingham B4 7XG, UK*

\**Xiao.Ai@bristol.ac.uk*

**Abstract:** The ability to observe the Earth's carbon cycles from space provides scientists an important tool to analyze climate change. Current proposed systems are mainly based on pulsed integrated path differential absorption lidar, in which two high energy pulses at different wavelengths interrogate the atmosphere sequentially for its transmission properties and are back-scattered by the ground. In this work an alternative approach based on random modulation single photon counting is proposed and analyzed; this system can take advantage of a less power demanding semiconductor laser in intensity modulated continuous wave operation, benefiting from a better efficiency, reliability and radiation hardness. Our approach is validated via numerical simulations considering current technological readiness, demonstrating its potential to obtain a 1.5 ppm retrieval precision for 50 km averaging with 2.5 W average power in a space-borne scenario. A major limiting factor is the ambient shot noise, if ultra-narrow band filtering technology could be applied, 0.5 ppm retrieval precision would be attainable.

Published by The Optical Society under the terms of the [Creative Commons Attribution 4.0 License](#). Further distribution of this work must maintain attribution to the author(s) and the published article's title, journal citation, and DOI.

**OCIS codes:** (010.3640) Lidar; (030.5260) Photon counting; (280.0280) Remote sensing and sensors; (280.1910) DIAL, differential absorption lidar; (140.5960) Semiconductor lasers

## References and links

1. G. Keppel-Aleks, J. T. Randerson, K. Lindsay, B. B. Stephens, J. K. Moore, S. C. Doney, P. E. Thornton, N. M. Mahowald, F. M. Hoffman, C. Sweeney, P. P. Tans, P. O. Wennberg, and S. C. Wofsy, "Atmospheric carbon dioxide variability in the community Earth system model: Evaluation and transient dynamics during the twentieth and twenty-first centuries," *J. Climate* **26**, 4447-4475 (2013).
2. G. Ehret, C. Kiemle, M. Wirth, A. Amediek, A. Fix, and S. Houweling, "Space-borne remote sensing of CO<sub>2</sub>, CH<sub>4</sub>, and N<sub>2</sub>O by integrated path differential absorption lidar: A sensitivity analysis," *Appl. Phys. B* **90**, 593-608 (2008).
3. P. Ingmann, P. Bensi, Y. Duran, A. Griva, and P. Clissold, "A-SCOPE – Advanced space carbon and climate observation of planet Earth," ESA Report for assessment, SP-1313/1 (2008).
4. J. B. Abshire, H. Riris, G. R. Allan, C. J. Weaver, J. Mao, X. Sun, W. E. Hasselbrack, S. R. Kawa, and S. Biraud, "Pulsed airborne lidar measurements of atmospheric CO<sub>2</sub> column absorption," *Tellus Ser. B* **62**, 770-783 (2010).
5. G. J. Koch, B. W. Barnes, M. Petros, J. Y. Beyon, F. Amzajerdian, J. Yu, R. E. Davis, S. Ismail, S. Vay, M. J. Kavaya, and U. N. Singh, "Coherent differential absorption lidar measurements of CO<sub>2</sub>," *Appl. Opt.* **43**, 5092-5099 (2004).
6. M. Wirth, A. Fix, P. Mahnke, H. Schwarzer, F. Schrandt, and G. Ehret, "The airborne multi-wavelength water vapor differential absorption lidar wales: System design and performance," *Appl. Phys. B* **96**, 201-213 (2009).
7. K. Numata, J. R. Chen, S. T. Wu, J. B. Abshire, and M. A. Krainak, "Frequency stabilization of distributed-feedback laser diodes at 1572 nm for lidar measurements of atmospheric carbon dioxide," *Appl. Opt.* **50**, 1047-1056 (2011).
8. H. Wenzel, S. Schwertfeger, A. Klehr, D. Jedrzejczyk, T. Hoffmann, and G. Erbert, "High peak power optical pulses generated with a monolithic master-oscillator power amplifier," *Opt. Lett.* **37**, 1826-1828 (2012).

9. P. Adamiec, B. Bonilla, A. Consoli, J. M. G. Tijero, S. Aguilera, and I. Esquivias, "High-peak-power pulse generation from a monolithic master oscillator power amplifier at 1.5  $\mu\text{m}$ ," *Appl. Opt.* **51**, 7160–7164 (2012).
10. M.-C. Amann, T. Bosch, M. Lescure, R. Myllyla, and M. Rioux, "Laser ranging: A critical review of usual techniques for distance measurement," *Opt. Eng.* **40**, 10–19 (2001).
11. J. T. Dobler, F. W. Harrison, E. V. Browell, B. Lin, D. McGregor, S. Kooi, Y. Choi, and S. Ismail, "Atmospheric CO<sub>2</sub> column measurements with an airborne intensity-modulated continuous wave 1.57  $\mu\text{m}$  fiber laser lidar," *Appl. Opt.* **52**, 2874–2892 (2013).
12. S. Kameyama, M. Imaki, Y. Hirano, S. Ueno, S. Kawakami, D. Sakaizawa, T. Kimura, and M. Nakajima, "Feasibility study on 1.6  $\mu\text{m}$  continuous-wave modulation laser absorption spectrometer system for measurement of global CO<sub>2</sub> concentration from a satellite," *Appl. Opt.* **50**, 2055–2068 (2011).
13. J. F. Campbell, "Nonlinear swept frequency technique for CO<sub>2</sub> measurements using a cw laser system," *Appl. Opt.* **52**, 3100–3107 (2013).
14. X. Ai, R. W. Nock, N. Dahnoun, J. Rarity, A. Consoli, I. Esquivias, M. Quatrevalet, and G. Ehret, "Pseudo-random single photon counting for space-borne atmospheric sensing applications," in *2014 IEEE Aerospace Conference* (IEEE, 2014) pp. 1–10.
15. B. Lin, A. R. Nehrir, F. W. Harrison, E. V. Browell, S. Ismail, M. D. Obland, J. Campbell, J. Dobler, B. Meadows, T.-F. Fan, and S. Kooi, "Atmospheric CO<sub>2</sub> column measurements in cloudy conditions using intensity-modulated continuous-wave lidar at 1.57 micron," *Opt. Express*, **23**(11), A582–A593 (2015).
16. P. Kapusta, M. Wahl, and R. Erdmann, *Advanced Photon Counting: Applications, Methods, Instrumentation* (Springer, 2015).
17. J. Beck, T. Welch, P. Mitra, K. Reiff, X. Sun, and J. Abshire, "A highly sensitive multi-element HgCdTe e-APD detector for IPDA lidar applications," *J. Electron. Mater.* **43**, 2970–2977 (2014).
18. M. Quatrevalet, X. Ai, A. Pérez-Serrano, P. Adamiec, J. Barbero, A. Fix, J. M. G. Tijero, I. Esquivias, J. G. Rarity, and G. Ehret, "Atmospheric CO<sub>2</sub> sensing with a random modulation continuous wave integrated path differential absorption lidar," submitted (2016).
19. N. Takeuchi, N. Sugimoto, H. Baba, and K. Sakurai, "Random modulation cw lidar," *Appl. Opt.* **22**, 1382–1386 (1983).
20. M. Faueron, M. Vilera, M. Krakowski, Y. Robert, E. Vinet, P. Primiani, J. P. L. Goëc, O. Parillaud, A. Pérez-Serrano, J. M. G. Tijero, G. Kochem, M. Traub, I. Esquivias, and F. van Dijk, "High power three-section integrated master oscillator power amplifier at 1.5  $\mu\text{m}$ ," *IEEE Photonics Technol. Lett.* **27**, 1449–1452 (2015).
21. J. G. Rarity, T. E. Wall, K. D. Ridley, P. C. M. Owens, and P. R. Tapster, "Single-photon counting for the 1300–1600-nm range by use of peltier-cooled and passively quenched InGaAs avalanche photodiodes," *Appl. Opt.* **39**, 6746–6753 (2000).
22. A. Pérez-Serrano, M. Vilera, I. Esquivias, M. Faueron, M. Krakowski, F. van Dijk, G. Kochem, M. Traub, P. Adamiec, J. Barbero, X. Ai, J. G. Rarity, M. Quatrevalet, and G. Ehret, "Atmospheric CO<sub>2</sub> remote sensing system based on high brightness semiconductor lasers and single photon counting detection," *Proc. SPIE* **9645**, 964503 (2015).
23. L. Rothman, I. Gordon, Y. Babikov, A. Barbe, D. C. Benner, P. Bernath, M. Birk, L. Bizzocchi, V. Boudon, L. Brown, A. Campargue, K. Chance, E. Cohen, L. Coudert, V. Devi, B. Drouin, A. Fayt, J.-M. Flaud, R. Gamache, J. Harrison, J.-M. Hartmann, C. Hill, J. Hodges, D. Jacquemart, A. Jolly, J. Lamouroux, R. L. Roy, G. Li, D. Long, O. Lyulin, C. Mackie, S. Massie, S. Mikhailenko, H. MÅijller, O. Naumenko, A. Nikitin, J. Orphal, V. Perevalov, A. Perrin, E. Polovtseva, C. Richard, M. Smith, E. Starikova, K. Sung, S. Tashkun, J. Tennyson, G. Toon, V. Tyuterev, and G. Wagner, "The HITRAN2012 molecular spectroscopic database," *J. Quant. Spectrosc. Radiat. Transfer* **130**, 4–50 (2013).
24. J. Caron and Y. Durand, "Operating wavelengths optimization for a spaceborne lidar measuring atmospheric CO<sub>2</sub>," *Appl. Opt.* **48**, 5413–5422 (2009).
25. J. F. Campbell, N. S. Prasad, and M. A. Flood, "Pseudorandom noise code-based technique for thin-cloud discrimination with CO<sub>2</sub> and O<sub>2</sub> absorption measurements," *Opt. Eng.* **50**, 126002 (2011).
26. R. Matthey and V. Mitev, "Pseudo-random noise-continuous-wave laser radar for surface and cloud measurements," *Opt. Lasers Eng.* **43**, 557–571 (2005).
27. COESA, *U.S. Standard Atmosphere, 1976* (U.S. Government Printing Office, 1976).
28. A. Amediek, A. Fix, G. Ehret, J. Caron and Y. Durand, "Airborne lidar reflectance measurements at 1.57  $\mu\text{m}$  in support of the A-SCOPE mission for atmospheric CO<sub>2</sub>," *Atmos. Meas. Tech.* **2**, 755–772 (2009).
29. B. Mayer and A. Kylling, "Technical note: The libRadtran software package for radiative transfer calculations - description and examples of use," *Atmos. Chem. Phys.* **5** 1855–1877 (2005).
30. D. Noordegraaf, P. M. W. Skovgaard, M. D. Nielsen, and J. Bland-Hawthorn, "Efficient multi-mode to single-mode coupling in a photonic lantern," *Opt. Express* **17**, 1988–1994 (2009).
31. T. A. Birks, I. Gris-Sánchez, S. Yerolatsitis, S. G. Leon-Saval, and R. R. Thomson, "The photonic lantern," *Adv. Opt. Photonics* **7**, 107–167 (2015).
32. E. Georgieva, W. S. Heaps, and W. Huang, "New broadband lidar for greenhouse carbon dioxide gas sensing in the Earth's atmosphere," *Proc. SPIE* **8182**, 81820H (2011).

## 1. Introduction

Carbon dioxide (CO<sub>2</sub>) is the major anthropogenic greenhouse gas contributing to global warming and climate change. Its concentration has recently reached the 400-ppm mark, representing a more than 40 % increase with respect to its level prior to the industrial revolution [1]. However, the exchanges of CO<sub>2</sub> between the atmosphere and the natural or anthropogenic sources/sinks at the Earth's surface are still poorly quantified. A better understanding of these surface fluxes, and in particular their regional distribution, is required for appropriate policy making. Two approaches may be used to achieve this. In the so-called bottom-up approach, databases of known sources and sinks and their estimated magnitudes are compiled and totaled to assess regional fluxes. In the so-called top-down approach, the surface fluxes of CO<sub>2</sub> are derived from the observed spatial and temporal gradients in atmospheric concentration using inverse modeling. Only the top-down approach provides a truly independent assessment of the surface fluxes, but it requires a sufficiently dense and evenly distributed set of global observations, which the current global network of in-situ measurements at surface stations cannot provide. This is why various satellite missions focusing on global mapping of atmospheric CO<sub>2</sub> have been proposed and, in some cases, launched in the past decade. In addition to passive measurement techniques, the integrated path differential absorption (IPDA) lidar technique [2] has been found to be potentially suited for fulfilling the stringent observational requirements. It uses strong CO<sub>2</sub> absorption lines in the 1.57 or in the 2 μm region and backscatter from the ground or a cloud top to measure the column averaged CO<sub>2</sub> mixing ratio (*XCO<sub>2</sub>*) with high precision and accuracy. The European Space Agency (ESA), in particular, has studied this concept in the frame of the Advanced Space Carbon and Climate Observation of Planet Earth (A-SCOPE) mission in 2006. Although a lack of technological readiness prevented its selection for implementation, recommendations were formulated to mature the instrument concept by pursuing technological efforts [3]. In addition, in recent years a tremendous effort has been put forth in the assessment of the optimal CO<sub>2</sub> active sensing methodology in the context of NASA mission Active Sensing of CO<sub>2</sub> Emissions over Nights, Days, and Season (ASCENDS) [4].

The availability of suitable laser sources is one of the main challenges in future space missions for atmospheric remote sensing. Typical laser sources currently used in Differential Absorption lidar (DIAL) systems are solid state lasers working in a pulsed regime, emitting ns pulses with high energy at a low to medium repetition rate (typical values are 10-50 ns, 10-50 mJ, 50-200 Hz) [5, 6]. Although these laser systems have demonstrated high average power, good beam quality and frequency stability required by the application, it is at the expense of a bulky system with low wall-plug efficiency, which is a main concern for space-borne applications. Hybrid Master Oscillator Power Amplifiers (MOPAs), based on a Distributed Feedback (DFB) semiconductor laser acting as a seed laser and an Erbium Doped Fiber Amplifier (EDFA) working in pulsed conditions, have been investigated in the context of ASCENDS [7]. However, the use of active optical fibers in space applications requires specific attention to radiation shielding, orbit and the duration of the flight. All-semiconductor laser sources are very interesting candidates for space-borne atmospheric sensing applications, due to their compactness, high efficiency, reliability and radiation hardness. Monolithically integrated MOPAs have reached 12 W in CW operation and 42 W in pulsed operation at 1064 nm [8] and 1.6 W in CW operation and 2.7 W in pulsed operation at 1550 nm [9]. However, they cannot produce the high energy pulses needed in a standard pulsed IPDA lidar. Instead they are very well suited to intensity modulated continuous wave (IM-CW) techniques [10]. These techniques have been proposed to perform atmospheric CO<sub>2</sub> sensing, including linear swept sine wave CW [11], unswept sine wave CW [12], nonlinear swept sine wave CW [13] and random modulated CW (RM-CW) [14]. Air-borne CO<sub>2</sub> measurements using IM-CW linear swept sine wave CW using hybrid MOPAs have been demonstrated in the context of ASCENDS [11, 15].

All these IPDA techniques, pulsed and IM-CW, can benefit by using Single Photon Counting

(SPC) techniques in the receiver [16]. In fact, photomultiplier detectors have been used in pulsed systems [4] and HgCdTe Avalanche Photodiodes (APD) have been proposed for the application [17]. However, SPC techniques are specially suited for enhancing IM-CW systems due to their low peak power. In particular, we have recently demonstrated the feasibility of CO<sub>2</sub> concentration IPDA measurements with a RM-CW system and a SPC receiver [18]. These promising results were performed in a horizontal path at ground level open up the possibility of using this technology in the space-borne scenario. Here, the parametric analysis of a RM-CW IPDA lidar system with a SPC-based receiver is performed in order to provide the guidelines for its space-borne implementation.

In this paper, a numerical model is presented, including the analysis of wavelength-dependent parameters for an optimal selection of on- and off-line wavelength; estimation of the expected signal and ambient light photon arrival rate and dynamic range, for a clear definition of the detector specification; study of the Signal-to-Noise Ratio (SNR) impact of topographic changes during integration time. The model has then been tested extensively, ensuring to yield the best system configuration in terms of attainable CO<sub>2</sub> retrieval precision (random error). All system parameters and operation conditions are bounded by existing technology readiness, yielding to a precision of 1.5 ppm or 0.36% for a low reflectivity value as given by water surfaces in order to meet the scientific requirements set by the A-SCOPE specification for global CO<sub>2</sub> observations from space [3]. It has been identified that the ambient shot noise places an ultimate upper-bound to further improvements; hence, in the last part of this paper, a review of suitable ultra-narrow band (< 100 pm) filtering technologies is included, with the potential for this filtering technology to allow for a 0.5 ppm precision.

The paper is organized as follows, in Section 2 an overview of the proposed space-borne RM-CW SPC IPDA lidar system is presented. The model is derived in detail in Section 3 and its analysis with respect to their most important parameters is described in Section 4. The accuracy improvement based on suitable filtering technologies is discussed in Section 5. Finally, the conclusions are summarized in Section 6.

## 2. Space-borne RM-CW SPC IPDA lidar system concept overview

A space-borne IPDA lidar measures the ratio of the atmospheric transmittances at two wavelengths to calculate  $XCO_2$ , one close to the CO<sub>2</sub> absorption line (on-line) and another away from the absorption line (off-line) (see Fig. 1(a)). Conventional pulsed systems measure the transmittances through laser pulse returns back-scattered by the ground surface. To avoid ambiguity, pulses are sent sequentially separated with the round-trip time-of-flight from satellite to ground, which may lead to bias in the measurements due to on-line/off-line footprint misalignments. These problems are avoided by using the so-called RM-CW or Pseudo-Random Noise (PRN) modulation approach [19]. In a RM-CW IPDA lidar, the on-line wavelength signal is modulated with a Pseudo Random Bit Sequence (PRBS), while the off-line wavelength signal is modulated with the same PRBS but delayed, then the signals are mixed and sent to the atmosphere. Both wavelength signals are transmitted simultaneously thus avoiding misalignment problems. The returned signal reflected from the ground surface is correlated with the original PRBS in order to retrieve the path length and the CO<sub>2</sub> concentration as shown in Fig. 1(b).

The system schematic of the proposed space-borne RM-CW SPC IPDA lidar is illustrated in Fig. 1(c). The various system parameters have been obtained by the simulation studies that will be detailed in Section 4. The lasers for the on- and off-line channels are monolithically integrated three-section MOPAs, each one containing a distributed feedback DFB section, a modulator section and a tapered amplifier [20]. Three separate electrical contacts have access to the three sections on the laser chip: the DFB current controls the laser emission frequency, the modulation current allows for intensity modulation and generation of the PRBS and the tapered amplifier current for providing the signal amplification. An optical-electrical feedback loop, the so-called

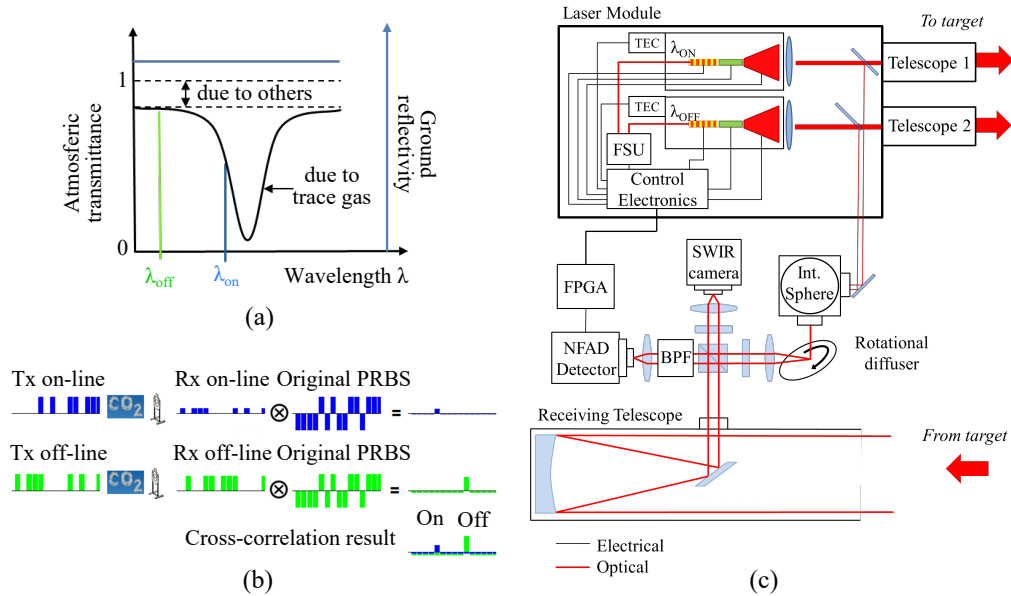


Fig. 1. (a) Position of the on-line  $\lambda_{on}$  and off-line  $\lambda_{off}$  selected wavelengths with respect to the CO<sub>2</sub> absorption line. The absorption line chosen is around 1572.018 nm in order to minimize the interference from the H<sub>2</sub>O lines. (b) RM-CW IPDA lidar principle. A PRBS for the on-line and the same PRBS delayed for the off-line are transmitted through the atmosphere. The received signals are correlated with the original bipolar sequence, from the cross-correlation result the *DAOD* can be obtained. (c) Proposed space-borne RM-CW SPC IPDA lidar system based on two 3-section monolithically integrated MOPAs [20].

Frequency Stabilization Unit (FSU), based on a gas cell reference is used in each laser chip in order to have highly stable emission frequencies and narrow linewidths.

Both wavelength signals are combined and then transmitted through a beam expander with an output divergence of 50  $\mu$ rad. The modulation bit rate is set to 25 Mb/s (clock period of 40 ns), which provides a distance resolution of 6 m. The backscattered light (referred as the received on- and off-line channels) is collected by a reflective telescope with a field-of-view slightly greater than the laser beam divergence (55  $\mu$ rad) [12]. The collimated light then passes through a narrow band interference filter with 500 pm Full Width at Half Maximum (FWHM) bandwidth, before being focused onto a single photon detector. The measurement of the Differential Absorption Optical Depth (*DAOD*) involves not only the on- and off-line energy of the received channels but also the accurate measurement of the emitted energy via the transmission channels. Such measurements can be taken from sampling the combined beams via mirror back-leakage and an integrating sphere (for the purpose of homogenizing and attenuation). A short wave infrared (SWIR) camera is used for aligning the emitted and received spots to the detector. At the single photon detector [21], incident photons trigger an avalanche event, which outputs an electrical pulse. These pulses are then cross-correlated with the transmitted PRBS resulting in range resolved returns that are equivalent to those obtained in a backscattered pulsed system. In the resulting cross-correlation, the last return bins record the total received photon number for the on- and off-line wavelengths  $R_{on,off}$ ; their positions indicate the distance to the ground surface, and the sample of the emitted energies are recoded at the initial bins as the photon numbers  $E_{on,off}$ . All digital domain signal processing can be implemented in a singular radiation hardened Field Programmable Gate Array (FPGA). We refer the reader to [18,22] for further details.

### 3. Space-borne lidar model

#### 3.1. Basic system model framework

We apply the RM-CW approach, which is capable of obtaining range resolved intensity measurements of simultaneously transmitted on- and off-line wavelengths returns. A model is built to evaluate the CO<sub>2</sub> retrieval precision under influence of various system parameters and operating conditions. The principle of the RM-CW or PRN modulation is that the cross-correlation of an  $N$ -bit pseudo-random binary sequence PRBS  $a[i] \in \{0, 1\}$  with its bipolar sequence described by  $\tilde{a}[i] = 2a[i] - 1 \in \{-1, 1\}$ , only has a value at zero shifts but close to zero elsewhere. For  $N \gg 1$ , it can be written as

$$a[i] \otimes \tilde{a}[i] \approx \frac{N}{2} \delta[i], \quad (1)$$

where  $\delta[i]$  is the discrete unit impulse function or Kronecker delta ( $\delta_{i,0}$ ). When the transmitted optical power is modulated with a PRBS  $a[i]$  of a bit time (or chip-time)  $T_c$ , the cross-correlation result reveals the received signal with its peak indicating the return being backscattered at a distance  $Z = c\tau/2$ , being  $\tau$  the time-of-flight (TOF). In the case of IPDA, the emitted signals with average power  $P_{on,off}$  are coded separately with sequences  $a_{on,off}[i]$ . The received signal will be dominated by the ground surface reflection that experiences a delay of  $\tau$  and signals are weakened by a factor  $G_{on,off}$ . This results in the received echo photo-electron counts per sample  $n_{on,off}[i]$  as

$$n_{on,off}[i] = 2T_c \eta_e P_{on,off} G_{on,off} a_{on,off} \left[ i - \left\lfloor \frac{\tau}{T_c} \right\rfloor \right], \quad (2)$$

where  $\eta_e$  denotes the conversion coefficient from total photon energy to detections of photo-electrons,  $\eta_e = \lambda \eta_{ph} / (hc)$ , where  $\eta_{ph}$  is the optical and quantum efficiency,  $h$  is the Planck's constant and  $c$  is the speed of light in vacuum;  $\lfloor x \rfloor$  denotes the integer part function and

$$G_{on,off} = \alpha \frac{A_r}{Z^2} e^{-2OD_{on,off}}, \quad (3)$$

where  $\alpha$  is the albedo for the ground (approximated by a Lambertian surface),  $A_r$  is the receiving telescope area,

$$OD_{on,off} = OD_0 + \int_0^Z \sigma_{on,off}(z) n_{co2}(z) dz, \quad (4)$$

is the total column optical depth, which includes a wavelength-independent losses term due to aerosols,  $OD_0 = \int_0^Z \beta_a(z) dz$ , with  $\beta_a(z)$  denoting the aerosol extinction ratio profile. The CO<sub>2</sub> optical depth (last term in RHS of Eq. (4)), is related to the altitude  $z$  dependent effective absorption cross-section  $\sigma_{on,off}(z)$  and that of the number density  $n_{co2}(z)$ . The single photon cross-correlation at the receiver can be written as

$$C_{on,off}[i] = n_{on,off}[i] \otimes \tilde{a}_{on,off}[i]. \quad (5)$$

For the space-borne scenario, it is assumed that during each sample time (equal to the chip time  $T_c$  of the PRBS), the probability of photon arrival is less than 1. Consequently, the cross-correlation can be inferred as the summation of correlated counts gated by the delayed versions of  $\tilde{a}_{on,off}$ . The correlated counts from ground reflections  $R_{on,off}$  can be then described as

$$R_{on,off} = C_{on,off} \left[ \left\lfloor \frac{\tau}{T_c} \right\rfloor \right] = NT_c \eta_e P_{on,off} G_{on,off}. \quad (6)$$

The differential absorption optical depth is denoted as  $DAOD = OD_{on} - OD_{off}$ . It quantifies the molecular absorption by the  $CO_2$  along the path between the scattering surface and the instrument. It can be obtained according from Eqs. (3) and (4) as

$$DAOD = \frac{1}{2} \ln \left( \frac{E_{on} R_{off}}{E_{off} R_{on}} \right) = \int_0^Z (\sigma_{on}(z) - \sigma_{off}(z)) n_{co2}(z) dz, \quad (7)$$

where  $E_{on,off}$  are the cross-correlation peaks corresponding to the reference of the transmitted on- and off-line signals and  $R_{on,off}$  are obtained from the peaks corresponding to the received echoes. At any altitude, the quantity of scientific interest, the dry-air volume mixing ratio of  $CO_2$ ,  $vmr_{co2}$ , is related to  $n_{co2}$  and number density of dry air  $n_{air}$  via  $vmr_{co2}(z) = n_{co2}(z)/n_{air}(z)$ . Thus, by rewriting Eq. (7), it can be shown that the lidar measured quantity  $DAOD$  is proportional to a weighted average of  $vmr_{co2}$  over the whole column as

$$XCO_2 = \frac{\int_0^Z vmr_{co2}(z) WF(z) dz}{\int_0^Z WF(z) dz} = \frac{DAOD}{IWF}, \quad (8)$$

where

$$WF(z) = n_{air}(z) (\sigma_{on}(z) - \sigma_{off}(z)), \quad (9)$$

is often referred to as the weighting function, the proportionality factor between  $XCO_2$  and  $DAOD$  is the integral of  $WF(z)$  over the whole column,  $IWF = \int_0^Z WF(z) dz$ . According to the ideal gas law, the profile can be calculated as

$$n_{air}(z) = \frac{A_v p(z)}{k_B T(z)}, \quad (10)$$

where  $A_v$  denotes the Avogadro's number,  $k_B$  is the Boltzmann's constant,  $p(z)$  and  $T(z)$  denote pressure and temperature profiles respectively.

As shown by the large body of theoretical and laboratory work that enables the compilation of extensive line-by-line spectroscopic databases such as HITRAN [23], the absorption lines of  $CO_2$  (along with many other trace gases) can be characterized very accurately, so that the altitude dependent absorption cross-section  $\sigma_{on,off}(z)$  may be calculated as a function of the pressure and temperature at the considered altitude. Furthermore, pressure and temperature profiles may be extracted from Numerical Weather Prediction (NWP) models, along with water vapor profiles which also make it possible to calculate the number density of dry air at each altitude as well. Thus,  $IWF$  may be calculated independently from the instrument's  $DAOD$  measurement itself and the latter converted to  $XCO_2$ . To summarize,  $XCO_2$  can be calculated from the following information: (a) the instrument measured  $DAOD$  by the energy ratio of the received on- and off-line wavelengths; (b) the orbit altitude to ground distance  $Z$ , also derived from the lidar returns themselves; and (c) NWP and spectroscopic auxiliary data. By proper selection of the sounding on- and off-line wavelengths possible measurement biases due to atmospheric water vapor can be significantly reduced [24].

### 3.2. Effective absorption cross-section

The previous sections assume the laser light is monochromatic, the line-shape of the laser is a perfect delta function without drift, and modulation yields to zero broadening. Impacts of these factors need to be taken into consideration in the model. The  $CO_2$  absorption process of the laser beam can be considered as the absorption cross-section convolved with the laser spectrum (characterized by its center and line-shape). The term, effective absorption cross-section has been applied to describe this phenomenon replacing  $\sigma_{on,off}$  in Eq. (9), which is obtained by

convolving the absorption cross-section spectrum of the CO<sub>2</sub> by the laser power spectrum at both wavelengths  $\tilde{P}_{on,off}(\lambda)$ , denoted by

$$\tilde{\sigma}_{on,off} = \int_0^{\infty} \sigma(z, \lambda) \tilde{P}_{on,off}(\lambda) d\lambda, \quad (11)$$

where

$$\tilde{P}_{on,off}(\lambda) = \frac{1}{\sigma_{\lambda} \sqrt{2\pi}} e^{-\frac{1}{2} \left( \frac{\lambda_{on,off} - \lambda}{\sigma_{\lambda}} \right)^2}, \quad (12)$$

in this case, the intrinsic laser linewidth (Voigt profile) combined with modulation broadening of a band-limited PRBS signal is simplified to be represented by a Gaussian density function, in which, the width of the broadened line-width is determined by  $\sigma_{\lambda}$ . Analysis of the laser frequency drift can be done applying offsets to the line center frequencies  $\lambda_{on}$  and  $\lambda_{off}$ . Because the focus of this work is centered around random errors, systematic errors such as drift are not taken into consideration in the analysis.

### 3.3. Simultaneous on- and off-line transmission and the ambient light

In order to transmit both lines' powers simultaneously, different modulation codes can be used, it is important that these codes need to be mutually orthogonal to avoid channel cross-talks. One option is to cyclically shift the on-line code to produce the off-line code [25], due to the fact that there is no backscattering from orbit altitude to the top of the atmosphere, the maximum non-ambiguous distance is the atmospheric depth (referring to the maximum delay of  $i_m$ ), when PRBS  $a[i]$  of the length  $N = 2i_m$  is used for the on-line:  $a_{on} = a[i]$ , the off-line code can be obtained by cyclically shifting the PRBS,  $a_{off} = a[i - i_m]$ . This approach allows the returns of both wavelengths to be separated and distinguishable in the cross-correlation result. At the detector, apart from the signal counts, ambient light and detector dark counts are also collected. The combined cross-correlation result  $C[i]$  is thus expanded from Eq. (5) to

$$C[i] = (n_{on}[i] + n_{off}[i] + n_{amb}[i] + n_{det}[i]) \otimes \tilde{a}[i]. \quad (13)$$

These extra counts are invariant with time and have no correlation to the PRBS, thus they produce no biases to the echo measurements. However, they introduce shot noise to the measurements that need to be quantified for the SNR calculations. Governed by the quantum nature of the single photon detection, it has been identified that the major noise contribution will be detector dark counts and shot noise induced by the ambient light. With a detector dark count rate of  $k_{dc}$  counts per second, the per sample detector dark count is  $n_{det} = k_{dc} T_c$  and that of the ambient light is quantified by

$$n_{amb} = L_s \eta_e T_c \Delta_{\lambda} A_s \frac{A_r}{Z^2} e^{-OD_0}, \quad (14)$$

where,  $L_s$  denotes the Nadir solar spectral radiance;  $\Delta_{\lambda}$  represents the bandwidth of the optical filter at the detector;  $A_s$  is the ground surface area covered by the detector field-of-view, that relates to the receiver field-of-view  $\theta_{FOV}$  of the receiver by  $A_s = \pi \theta_{FOV}^2 Z^2 / 4$ ;  $A_r / Z^2$  denotes the solid angle of the receiver telescope. The total dark counts and ambient counts integrated in a cross-correlation bin can be further denoted as  $R_{amb} = N n_{amb}$  and  $R_{det} = N n_{det}$  respectively.

### 3.4. SNR analysis and retrieval precision estimation

For shot noise limited SNR estimation, variance of the noise is related to the photo-electron collected. Poisson statistics govern the measurement, therefore the SNR can be written as [26]

$$SNR_{on,off} = \frac{R_{on,off}}{\sqrt{\sum_k V_k}}, \quad (15)$$

where  $\sum_k V_k = V$  takes into account all noise contributions. The variance  $V$  can be written as

$$V = R_{on} + R_{off} + R_{amb} + R_{det} . \quad (16)$$

The counts  $E_{on}$  and  $E_{off}$ , references for the emitted laser powers, are not taken into account in the SNR calculations as they drift slowly with time. In consequence,  $E_{on}$  and  $E_{off}$  can be adjusted to a significantly lower power (photon number) than that of the received signals  $R_{on}$  and  $R_{off}$ , and then their impact in the variance is negligible. A longer averaging time is used for the reference signals to correct possible shifts. Consequently the on- and off-line SNRs can be estimated as

$$SNR_{on,off} = \frac{R_{on,off}}{\sqrt{R_{on} + R_{off} + R_{amb} + R_{det}}} . \quad (17)$$

With the SNRs formulated, assuming Gaussian approximation to Poisson noise, the CO<sub>2</sub> retrieval precision can be estimated by Gaussian error propagation. Propagating the error in Eq. (7), the CO<sub>2</sub> detection precision can be written as

$$\delta XCO_2 = \sqrt{\left[ \left( \frac{\partial XCO_2}{\partial R_{on}} \right)^2 + \left( \frac{\partial XCO_2}{\partial R_{off}} \right)^2 \right] V} = \frac{\sqrt{SNR_{on}^{-2} + SNR_{off}^{-2}}}{2 IWF} . \quad (18)$$

### 3.5. Topographic variation during cross-correlation and along-track averaging

In the proposed system, cross-correlation is implemented as a gated accumulation of photoelectron numbers, and thus can be referred as integration. Longer integration time leads to a higher SNR value. For the system to detect the on- and off-line echoes with high accuracy, a minimum SNR of 10 requires an integration time of milliseconds. During this integration time, the topographic variation would be smaller than one range bin ( $cT_c/2$ ) for the ocean surface; in this case, the returned signal energy does not spread into multiple range bins in the cross-correlation result. However, on land, topographic variation during integration needs to be considered. As in this case, the signal energy spreads over a number of range bins denoted by  $N_{top}$ . To obtain an unbiased estimation of the mixing ratio, we propose to use a weighted average of the received power over the spread range bins as follows: after the millisecond integration time,  $XCO_2[i]$  is calculated for each range bin within the spread using the data acquired in the cross-correlation results  $C[i]$ . These are then averaged with the inverse of the estimated variance  $(\delta XCO_2[i])^{-2}$  as the weighting coefficient to obtain the weighted mean mixing ratio  $\langle XCO_2 \rangle$  as

$$\langle XCO_2 \rangle = \frac{\sum_{i=1}^{N_{top}} (\delta XCO_2[i])^{-2} XCO_2[i]}{\sum_{i=1}^{N_{top}} (\delta XCO_2[i])^{-2}} . \quad (19)$$

The precision is bounded by the square root of the spreading of bins, hence  $\delta \langle XCO_2 \rangle < \sqrt{N_{top}} \delta XCO_2$ . The SNR is then further improved by averaging over several seconds to achieve the required ppm CO<sub>2</sub> retrieval precision, such that along-track averaged mixing ratio is obtained as

$$XCO_2 = \frac{\sum_{i=1}^{N_{track}} \langle XCO_2[i] \rangle}{N_{track}} , \quad (20)$$

and the final retrieval precision can be approximated by  $\delta XCO_2 = \delta \langle XCO_2 \rangle / \sqrt{N_{track}}$ , where the number of weighted means to be averaged along track is denoted by  $N_{track}$ .

## 4. Analysis

### 4.1. Input datasets

The main geophysical inputs to the system model are shown in Fig. 2. These include altitude resolved pressure, temperature and aerosol extinction ratio. The US-standard atmosphere [27]

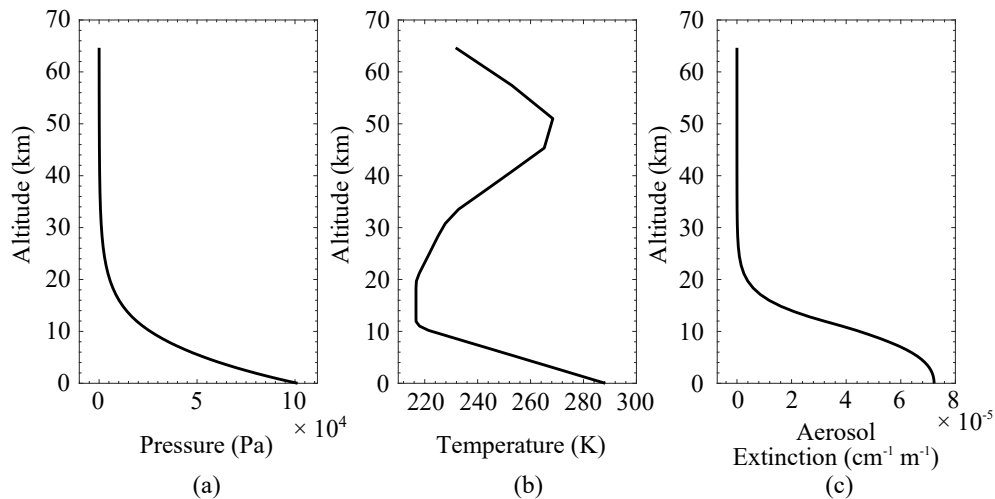


Fig. 2. (a) Pressure and (b) temperature profiles obtained as nominal values from US-standard atmosphere model. (c) Aerosol extinction profile, which is highly concentrated at low altitude.

is used to calculate the temperature and pressure profiles, and the number density of the  $\text{CO}_2$  is generated for this atmospheric state with the concentration at the current ground nominal value of 410 ppm. Discrete data input datasets sampled at exponentially spaced altitude grids are read into the model, and the trapezoid rule was applied for approximating the defined integrals in the calculations. As far as the aerosols are concerned, their variability is very high in the atmosphere; a median case is applied in this work. Other data inputs are included as follows. The standard surface reflectivity [28] and solar background spectral radiance [29] for ocean are  $0.03 \text{ sr}^{-1}$  and  $1.7 \text{ mWm}^{-2}\text{sr}^{-1}\text{nm}^{-1}$  respectively, those of the vegetation are  $0.1 \text{ sr}^{-1}$  and  $5.4 \text{ mWm}^{-2}\text{sr}^{-1}\text{nm}^{-1}$ , those of the desert are  $0.5 \text{ sr}^{-1}$  and  $15.7 \text{ mWm}^{-2}\text{sr}^{-1}\text{nm}^{-1}$ . In the context of A-SCOPE it was chosen to size the instrument for the ocean reflectivity, targeting for a threshold of 1.5 ppm. Both Mie and Rayleigh scattering are not considered in this model, due to their insignificance compared to the surface returns.

The absorption cross-section is obtained from the HITRAN database for the given atmospheric state, with a Voigt line profile, spanning from 1571.995 to 1572.026 nm and across the whole atmospheric depth as shown in Fig. 3, which shows the effects of altitude related linewidth broadening and center shifting towards the lower atmosphere. It has been shown in several studies [2] that placing the on-line at the wing of the absorption rather at the peak, can improve sensitivity towards the ground surface, where the contrasts in  $\text{CO}_2$  concentration due to local sources and sinks are strongest.

#### 4.2. Optimization method

The theoretical model presented in Section 3 defines the  $\text{CO}_2$  retrieval precision  $\delta X_{\text{CO}_2}$  (random error) in relation to varying system parameters. An extensive study of the model led to a good understanding of the underlying principles, yielding to a baseline system configuration. To optimize a large set of related parameters, an initial condition was defined. This is set according to the intuitive understanding of the IPDA lidar approach with reference to pulsed systems from [2]. Furthermore, the specifications suggested in the A-SCOPE report [3] were taken into consideration, bounding them according to current technological readiness and environmental

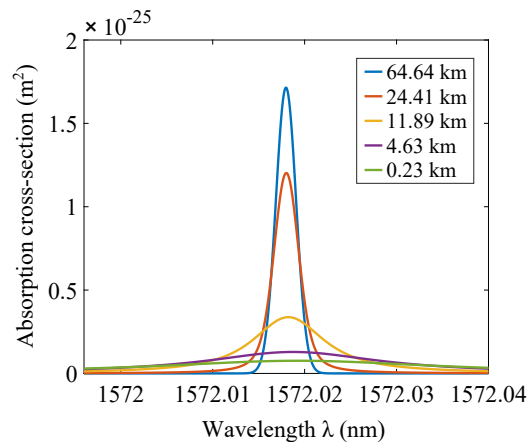


Fig. 3. Absorption cross-section spectra across the atmospheric depth.

and mission budget constraints. The methodology is to optimize the system with several iterations, starting from the initial configuration. Within each iteration, parameters are ranked by their importance and are then individually tuned sequentially. The resultant baseline system configuration and operating conditions are listed in Table 1. In the following sections, various parameters deviating from the baseline configuration and nominal operating conditions are studied in detail, considering power, size and reliability constraints.

#### 4.3. Results and discussion

The model estimates a 50 km along-track averaged retrieval precision with respect to the system parameters. Figure 4 shows the  $\text{CO}_2$  detection precision  $\delta X_{\text{CO}_2}$  for the three considered surfaces (ocean, vegetation and desert). A dashed line indicates the 1.5 ppm threshold set by the A-SCOPE specification [3].  $\lambda_{\text{off}}$  selection is uncritical for detection precision; 1571.995 nm was used in the baseline configuration as it is close enough to the  $\lambda_{\text{on}}$  to enable narrow band filtering.  $\lambda_{\text{on}}$  selection for optimal retrieval precision is shown in Fig. 4(a). If the line center was selected instead of the line wing, the retrieval precision would be much worse, resulting from excessive attenuation of the on-line signal. Further away from the symmetrical optimal positions in the wings of the line, the contrast between on-line and off-line signal becomes too small, worsening the precision. Figure 4(b) shows the gain of precision with increasing on-line average power  $P_{\text{on}}$ . Figure 4(c) shows the effect of the dark count rate  $k_{\text{dc}}$  of the SPC detector in the detection precision. For the baseline configuration,  $\delta X_{\text{CO}_2} < 1.5$  ppm for  $k_{\text{dc}} < 70$  Mcps. Figure 4(d) shows the detection precision dependence on the optical filter bandwidth  $\Delta_\lambda$ . One can see that as consequence that the ambient light is the main limitation to perform the measurement, the use of narrow filters can improve the detection precision. For the parameters shown in Table 1, a  $\delta X_{\text{CO}_2} = 0.5$  ppm could be achieved by using a filter with  $\Delta_\lambda = 100$  pm.

In Fig. 5, trade-offs and the relationship between two parameters are shown. Figure 5 are contour plots where the horizontal and vertical axes represent the parameters that deviate from the baseline configuration, three contours shown in different colors represent the attainable retrieval precision of three types of surface reflectance (ocean, vegetation and desert). The desirable and threshold retrieval precisions are indicated as 1 ppm and 1.5 ppm respectively. Figure 5(a) points out that the off-line power  $P_{\text{off}}$  is not critical for the proposed system, evidenced by its insensitivity towards the contribution of improvements in the detection precision. This is because, in the RM-CW scheme, both on-line and off-line powers are transmitted simultaneously. The

Table 1. Baseline configuration and geophysical parameters

<b>Laser transmitter</b>		
On-line output power	$P_{on}$	2.5 W
Off-line output power	$P_{off}$	2 W
On-line wavelength	$\lambda_{on}$	1572.026 nm
Off-line wavelength	$\lambda_{off}$	1571.995 nm
PRBS chip time	$T_c$	40 ns
Beam divergence	$\theta_{div}$	50 $\mu$ rad
<b>Receiver and detector</b>		
Telescope type		Reflector telescope
Primary mirror size	$A_r$	1.8 m <sup>2</sup>
Receiver field-of-view	$\theta_{FOV}$	55 $\mu$ rad
Filter bandwidth	$\Delta_\lambda$	500 pm
Detector type		HgCdTe e-APD
Dark count	$k_{dc}$	100 kcps
Optical and quantum efficiency	$\eta_{ph}$	60 %
Conversion coefficient	$\eta_e$	$4.74 \times 10^{18}$ counts/J
<b>Platform and environment</b>		
Orbit type		Sun-synchronous dawn/dust
Orbit altitude	$Z$	450 km
Ground velocity	$v_{gnd}$	7 km/s
Acquisition time	$t_{acq}$	0.02 s
Along-track averaging time	$t_{track}$	7 s
Number of averaged acquisition	$N_{track}$	350
Pressure	$p$	Standard atmosphere
Temperature	$T$	Standard atmosphere
Aerosol extinction	$\beta_a$	Median profile
Ground mixing ratio	$x_{CO_2}$	410 ppm

higher return from the off-line becomes a noise contribution to the more informative on-line return signal. Hence in an optimized configuration, the transmit power of the off-line should be lower than that of the on-line. This is the reason that the off-line average power in the baseline configuration is set to  $P_{off} = 2$  W while the on-line power is  $P_{on} = 2.5$  W. Figure 4(d) evidences that the most influential system parameter apart from the laser power is the filter bandwidth. Figure 5(b) shows the detection precision for varying the filter bandwidth  $\Delta_\lambda$  and the receiver field-of-view  $\theta_{FOV}$ . Figure 5(c) shows the detection precision for varying the on-line output power  $P_{on}$  and the filter bandwidth  $\Delta_\lambda$ . The major development efforts for the future space-borne application, together with the improvement of the output power of semiconductor lasers, should be focused on reliable narrow band filtering technologies (see discussion in Section 5) to optimize the laser divergence; and aim to limit the field-of-view of the receiver. For the baseline configuration, we have made a realistic selection of a technologically achievable 500 pm interference filter and 55  $\mu$ rad field of view. Note that, the field-of-view is ultimately limited by the beam wandering effect induced by the turbulence of the atmosphere thus values below 50  $\mu$ rad may not be realistic. Figure 5(b) shows that with more advanced types of filtering technologies with  $\Delta_\lambda \leq 100$  pm, the field-of-view of the space-borne receiver can be widened to 150  $\mu$ rad to achieve 1 ppm, this would reduce the beam pointing requirement and allows for headroom for beam wandering. Figure 5(d) illustrates two cost factors of the mission, the

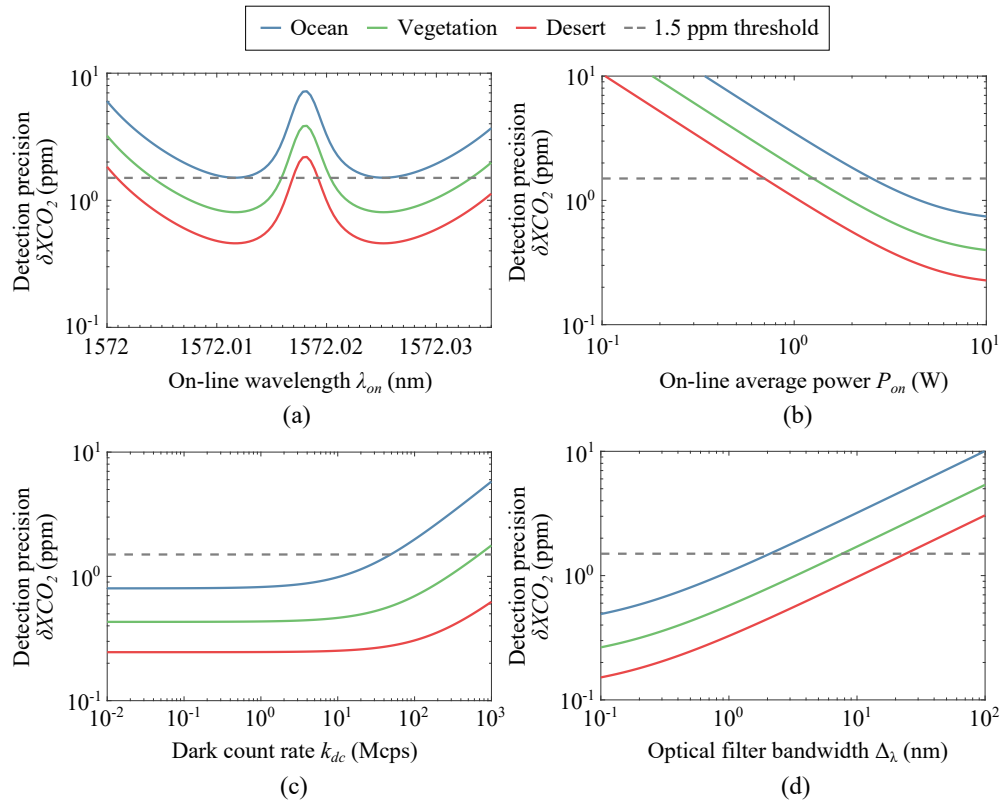


Fig. 4.  $CO_2$  detection precision ( $\delta X_{CO_2}$ ) for three types of surfaces with respect to a system parameter variation: (a) on-line center wavelength  $\lambda_{on}$ , (b) on-line average power  $P_{on}$ , (c) detector dark count rate  $k_{dc}$  and (d) optical filter bandwidth  $\Delta_\lambda$ . The dashed line represents the 1.5 ppm threshold set by the A-SCOPE specification [3].

telescope size and the orbit altitude. A lower orbit than the current 450 km is considered to be very costly and difficult due to the atmospheric draft encountered by the satellite. The telescope diameter of 1.5 m specified by the A-SCOPE maybe further improved through technological advancements. Finally we note that additional errors induced by uncertainty in atmospheric variables (temperature  $\delta T \approx \pm 1$  K, specific humidity  $\delta q \approx 10$  %, surface pressure  $\delta p_0 \approx \pm 1$  hPa) are expected to be small. For the above selected on-line wavelength, these errors add to a sub-total of 0.29 ppm which is well below the 1.5 ppm requirement [3].

## 5. Suitable filtering technologies

As discussed in Section 4, suitable ultra-narrow band optical filtering technologies rejecting background radiation would improve the system retrieval precision significantly. The selected baseline configuration uses technologically achievable dielectric interference filters with 500 pm bandwidth. In Fig. 4(d), it has been shown that reduction in the bandwidth will lead to proportional improvement in the retrieval precision. If 100 pm filtering technologies are applicable, the ocean surface case retrieval precision of 0.5 ppm can be achieved and the system performance will be limited only by the shot noise of the on- and off-line signal. An ultra-narrow band filter will not only benefit the system performance, it also would relax the requirements for the dynamic range and saturation count rate of the single photon detector.

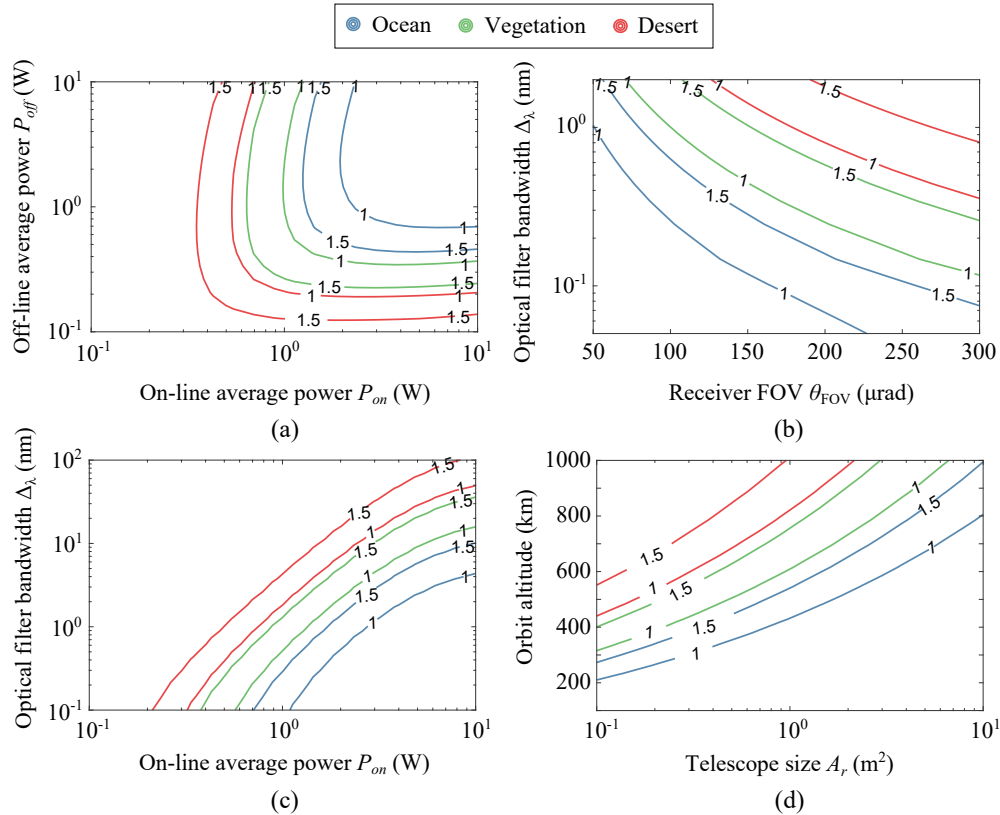


Fig. 5. CO<sub>2</sub> detection precision contour plots of three types of surface reflectance: ocean (blue), vegetation (green) and desert (red) where the horizontal and vertical axes represent the parameters that deviate from the baseline configuration: (a)  $P_{off}$  vs  $P_{on}$ , (b)  $\Delta\lambda$  vs  $\theta_{FOV}$ , (c)  $\Delta\lambda$  vs  $P_{on}$  and (d) Orbit altitude vs telescope size  $A_r$ . The desirable and threshold retrieval precisions are indicated as 1 ppm and 1.5 ppm respectively.

Several ultra-narrow band filtering technologies have already been applied or considered for space missions. One emerging technology is Fiber Bragg Gratings (FBG) that have been developed for the communication industry, readily available for 1572 nm L-band application, these are tunable and achieved FWHM lower than 100 pm. However, this technology is based on single mode fiber. Telescope to fiber coupling efficiency is small due to low mode coupling efficiency and beam wandering; this would render this approach ineffective. Aiming to solve the coupling problem, single mode fiber bundles has been used to form devices so-called photonic lanterns. In [30], 80  $\mu$ m multimode can be converted to 7 single mode fiber with a loss of 0.32 dB. In [31], one multimode fiber is converted to 120 single-mode cores with a photonic lantern, with FBG written in each core, then combined into an output multimode fiber. However, the FBG non-uniformity leads to a poor extinction, but this could be improved in the near future. A more matured technology that has been commonly applied in astronomy is the Fabry-Perot (FP) Etalon based filter. FP filters relies on multiple reflections between two spaced partially silvered surfaces. It is a simple device, but the key is to ensure perfect parallelism and surface smoothness of  $< \lambda/20$ . It is commonly available for solar viewing as H- $\alpha$  line filters (656 nm) for the mass market having a bandwidth of 0.7  $\text{\AA}$  (70 pm). Solid FP etalons are available custom made to specifications, readily available around 1572 nm, and tunable by temperature. Like

other optical cavity, FP Etalon has multiple resonances that are spaced by free spectral range FSR. They also have a Lorenz line shape rather than a flat top. In the IPDA lidar application, these resonances can be locked to the CO<sub>2</sub> absorption fringes, which has been achieved in one of NASA's broadband IPDA lidar [32].

## 6. Conclusion

Future space missions aim to accurately measure the CO<sub>2</sub> concentration utilizing space-borne IPDA lidars. In this paper, the simulation study results of a RM-CW SPC IPDA lidar system has been presented. In comparison to the sequential transmissions of the on-line and off-line wavelengths experienced in existing pulsed systems, the proposed instrument transmits both wavelengths simultaneously. Hence, the laser footprint misalignment problem can be eliminated. Furthermore, with a semiconductor CW source as an alternative to solid state pulsed ones, the proposed system can be more robust and should attain better wall-plug efficiency. The envelope SNR of the proposed system has been analyzed. Based on this analysis, optimized system parameters and setup arrangements are given in light of the existing technology. Although the proposed scheme may be more susceptible to ambient and detector noise, it has shown that for a low reflectivity case as given by the ocean surface, a retrieval precision of 1.5 ppm over 50 km path integration can be achieved assuming existing technological readiness. Advanced filtering technologies have been reviewed to mitigate the ambient light problem. The photonic lantern and FP based filters would allow sub-100 pm filtering hence allowing the retrieval precision to be improved to 0.5 ppm level. Future improvements can also be anticipated with the improvements in laser power. Taking advantage of their high wall-plug efficiency, 10 W averaged power could be achieved by a single or several semiconductor lasers in parallel to obtain even higher precision. This would also open the possibility for higher orbit micro-satellite missions for IPDA applications.

## Funding

This work was funded by the European Commission through the Seventh Framework Programme (BRITESPACE, 313200). A. Pérez-Serrano and I. Esquivias also acknowledge support from the Ministerio de Economía y Competitividad of Spain (RANGER, TEC2012-38864-C03-02; COMBINA, TEC2015-65212-C3-2-P); and the Comunidad de Madrid (SINFOTON-CM, S2013/MIT-2790). A. Pérez-Serrano acknowledges support from Ministerio de Economía y Competitividad (Ayudas a la Formación Posdoctoral 2013 program, FPDI-2013-15740).